A Closed-Loop, All-Electronic Pixel-Wise Adaptive Imaging System for High Dynamic Range Videography

Jie Zhang, *Member, IEEE*, Jonathan P. Newman, Xiao Wang, Chetan Singh Thakur, *Senior Member, IEEE*, John Rattray, *Student Member, IEEE*, Ralph Etienne-Cummings, *Fellow, IEEE*, and Matthew A. Wilson

***Abstract*— Digital cameras expose and readout all pixels in accordance with a global sample clock. This rigid global control of exposure and sampling is problematic for capturing scenes with large variance in brightness and motion, and may cause regions of motion blur, under- and overexposure. To address these issues, we developed a CMOS imaging system that automatically adjusts each pixel's exposure and sampling rate to fit local motion and brightness. This system consists of an image sensor with pixel-addressable exposure configurability in combination with a real-time, per-pixel exposure controller. It operates in a closed-loop to sample, detect and optimize each pixel's exposure and sampling rate for optimal acquisition. Per-pixel exposure control is implemented using all-integrated electronics without external optical modulation. This reduces system complexity and power consumption compared to existing solutions. Implemented using standard 130nm CMOS process, the chip has 256 × 256 pixels and consumes 7.31mW. To evaluate performance, we used this system to capture scenes with complex lighting and motion conditions that would lead to loss of information for globally-exposed cameras. These results demonstrate the advantage of pixel-wise adaptive.**

***Index Terms*— Image sensor, high dynamic range, exposure control, pixel-wise coded imaging.**

I. Introduction

IMAGE sensors are the "eyes" of computer vision systems found in many applications such as robotics, security and autonomous driving. Most image sensors use a frame-based architecture with global exposure that locks to the pixel readout timing [1]. This simple but effective architecture minimizes pixel size and improves sensitivity; however, its inability to adjust each pixel's exposure and frame rate independently can leads to sub-optimal sampling, especially for scenes with large dynamic range and motion. Fig. 1 shows some examples, where globally optimized exposure and sampling speed lead to regions of motion blur, under- and overexposure. Here, these captured video frames lose important information at the saturated and/or blurred regions, which propagates the errors to subsequent computer vision tasks such as motion estimation, object segmentation and recognition.

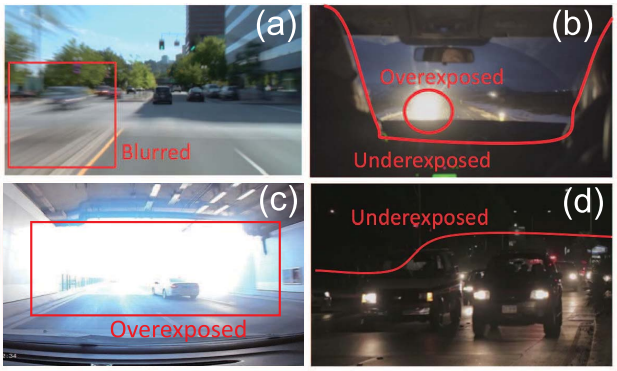

Fig. 1. Videos acquired with frame based image sensors. The highlighted area in the image are not optimally exposed: (a) Local motion blur due to low frame rate, (b-d) Under- and overexposure in image local regions due to global exposure. source: www.shutterstock.com.

In this work, we demonstrate an imaging system that solves sub-optimal pixel sampling by adapting each pixel's exposure and speed in real-time, according to local intensity and motion. Unlike frame-based image sensors, which can only optimize all pixels to a single setting, our image sensor's smallest adaptive units are pixels — each pixel can operate at different frame rate and exposure with complete freedom: some pixels can sample faster to capture high-speed motion, while others can slow down to prolong exposure for a dim region. The pixels settings are determined by a digital controller, which operates in a closed-loop with the image sensor to continuously optimize pixels' settings. This imaging system is compact and low-power due to all-CMOS implementation without using bulky optical modulators, in contrast to several previous works [2], [3].

The rest of the paper is organized as follows: We briefly discuss previous work in the area of high dynamic range (HDR)

Manuscript received July 5, 2019; revised October 13, 2019 and December 3, 2019; accepted January 28, 2020. Date of publication February 27, 2020; date of current version June 3, 2020. This work was supported in part by the National Eye Institute (NEI) under Grant R21EY028381 and in part by The Louis B. Thalheimer Fund for Translational Research. This article was recommended by Associate Editor V. J. Koomson. *(Corresponding author: Jie Zhang.)*

Jie Zhang, Jonathan P. Newman, and Matthew A. Wilson are with the Department of Brain and Cognitive Sciences, The Picower Institute for Learning and Memory, Massachusetts Institute of Technology, Cambridge, MA 02139 USA (e-mail: jzhang41@mit.edu).

Xiao Wang is with the Department of Computer Science, Boston University, Boston, MA 02215 USA.

Chetan Singh Thakur is with the Department of Electronic Systems Engineering, Indian Institute of Science, Bengaluru 560012, India.

John Rattray and Ralph Etienne-Cummings are with the Department of Electrical and Computer Engineering, Johns Hopkins University, Baltimore, MD 21218 USA.

Color versions of one or more of the figures in this article are available online at http://ieeexplore.ieee.org.

Digital Object Identifier 10.1109/TCSI.2020.2973396

and coded exposure imaging in section II. We then describe our adaptive pixel-wise imaging system in detail in section III, and follow up with experimental results in section VI. Lastly, we address some areas of improvement in discussion and conclude the paper in section V.

II. Summary of Previous Work

Several works provide non-integrated solutions for adaptively controlling of exposure patterns on conventional CMOS image sensors. Here, we review each class of these works:

Temporally varying exposure: To minimize imaging imperfection due to sub-optimal exposure, a conventional image sensor can be used to sequentially capture multiple images of the same scene at different global exposures [4]–[6]. Short exposure images capture details in bright regions while long exposure images enhance the signal quality in the dark regions. These sequential snapshots are then merged through tone-mapping algorithms to enhance overall scene dynamic range. While this method is widely used in photography, it is not suitable for non-stationary scenes as any movements during the sequential snapshots would cause ghosting in the tone-mapped HDR image. Furthermore, the need for multiple exposures limits the frame rate of the image sensor and can not be used for video applications.

Multiple image sensors: We can extend the above methods to videos by using a multi-sensor system to capture the scene at different exposure settings simultaneously [3], [7]. These setups use optical beamsplitters after the objective lens to generate multiple copies of the scene and then project them onto multiple detectors set at different exposures. While this method produces HDR frames in real-time, it requires multiple cameras and well-tuned/aligned optics. Furthermore, splitting the incoming light between two or more sensors attenuates collected light at each detector and degrades the Signal to Noise Ratio (SNR).

Spatially varying transmittance: Spatially modulating pixel transmittance can be used to enhance dynamic range without using multiple detectors [8], [9]. These methods use off-chip spatial light modulators (SLMs) prior to the image sensor to modulate incoming light intensity at each pixel. By placing an optical spatially varying transmittance mask across the focal plane, it allows local pixel groups to capture a wider dynamic range. However, this method requires spatial low pass filtering to generate the HDR scene, and results in loss of spatial resolution. In addition, this technique suffers from the added complexity of the off-chip SLM, which must be well aligned to each pixel.

Adaptive optical light intensity modulation: The optical transmittance mask can be coupled with a feedback control loop to modulate light intensity at pixel-level [2], [8]. These adaptive systems first detect over-exposed and/or poor illuminated regions within the scene. They then adjust incident light intensity at each pixel within the region to optimize the dynamic range. This method improves scene dynamic range without sacrificing spatial resolution, but drawbacks are the need for well-aligned optics, similar to other optically modulated methods. In addition, the image sensor's framerate is fixed, and when the pixel transmittance is at 100%, the system cannot extend exposure to further enhance SNR.

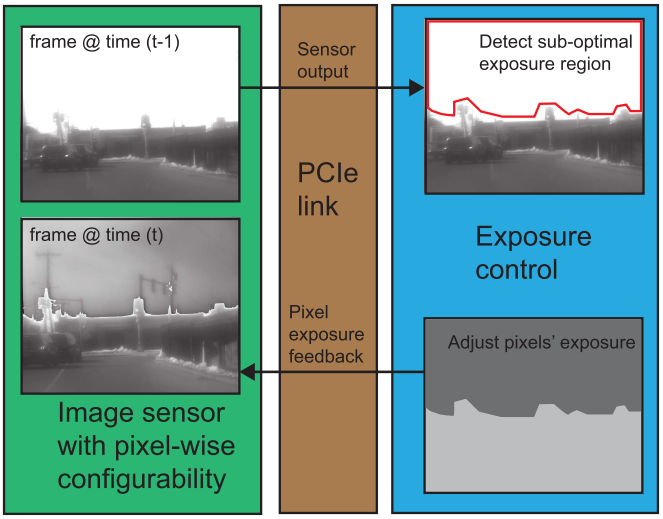

Fig. 2. The block diagram of our all-electronic pixel-wise exposure adaptive system. It consists of three parts: an image sensor with pixel-wise exposure configurability, a high speed bi-directional chip to computer interface using the PCIe bus, and real-time exposure control algorithms.

III. Pixel-Wise Adaptive Imaging System

Here we describe an adaptive imaging system that optimizes exposure and frame rate at the pixel level, achieves pixel-wise exposure control without external optical modulation. Fig. 2 illustrates the block diagram of this system, which has three parts: an image sensor with flexible pixel-wise exposure configurability, a high-speed chip computer bi-directional PCIe data link, and an exposure controller implemented off-chip on a computer. These three elements operate in a closed-loop to sample, detect and optimize each pixel's exposure and frame rate to enhance image quality. The PCIe link and the exposure controller can be integrated to a system-on-chip (SoC) solution to further decrease overall system size and power.

Fig. 2 also shows a this system's operation: The image sensor outputs frame 1 of a video at time (t-1). In this frame, the sky region of the scene is over-exposed which leads to saturation of important objects including poles and traffic lights. From this frame, the exposure controller then segments the region of sub-optimal exposure and re-calculates the desired exposure for every pixels. It feeds back the updated exposure to the image sensor, which then uses it to update the pixel configuration and sample the next frame at time (t), where both the sky and the road regions of the scene are optimally sampled. In this section, we describe each part of the system in detail.

A. Image Sensor With Pixel-Wise Exposure Configurability

A number of image sensors with pixel-wise exposure configurability have been demonstrated, including our previous work [10]–[12]. We first proposed a pixel-wise configurable exposure image sensor architecture [10]. However, as we shall

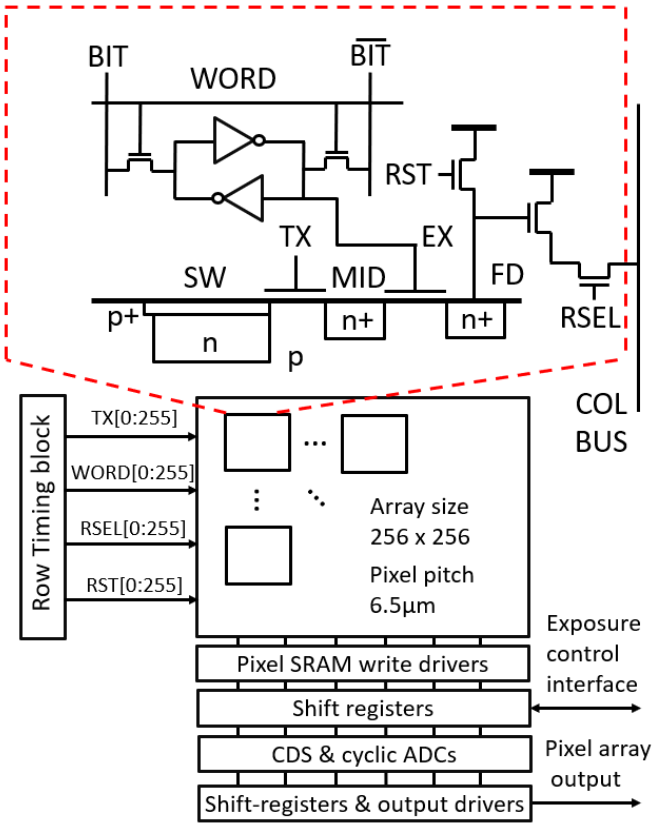

Fig. 3. Pixel-wise image sensor architecture. The sensor is fabricated in a standard 130nm CMOS process featuring an array of 256 × 256 pixels with 6.5μm pitch.

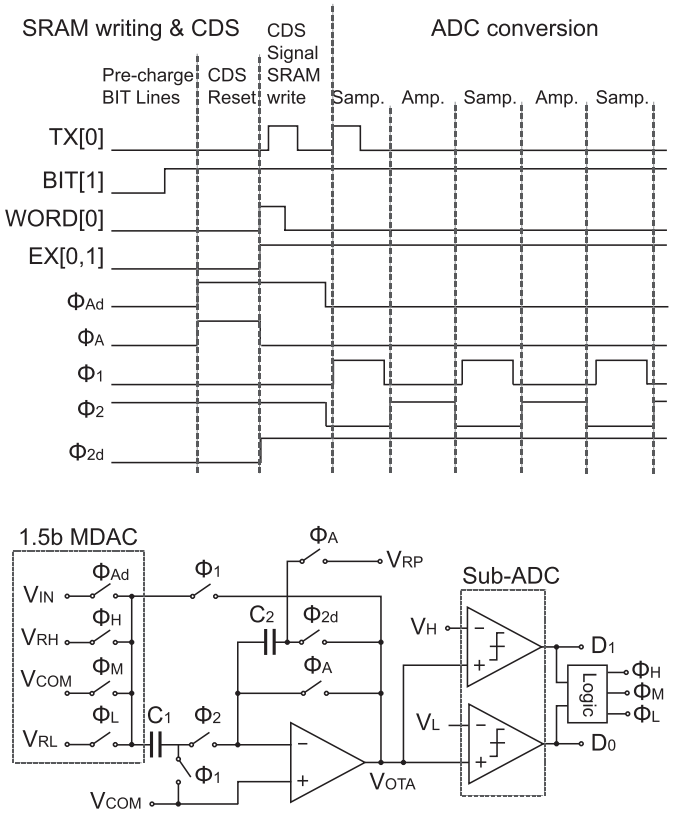

Fig. 4. An example pixel timing diagram and the schematic of the CDS and column cyclic ADC circuits.

discuss here in detail, this first design's timing causes small unintended sampling deadtime during exposure. Subsequently, Luo, Ho and Mirabbasi and Sarhangnejad et al. have proposed dual-tap approaches which use two floating diffusions (FD) to collect charges from the photodiode [11], [12]. Extra charge storage nodes allow for non-continuous coded exposure patterns that might be beneficial for Compressed Sensing. The disadvantage of this design is reduced light collection efficiency: The pixels either need extra readout circuits for both nodes, or it leaves photon induced charges in one of the nodes unmeasured. In this work, we improve on our previous design to ensure all the light-generated charges are accumulated during pixel exposure. The use of single-tap pixel improves fill factor and SNR.

1) Image Sensor Architecture: The image sensor design is outlined in Fig. 3. Fabricated using a standard 130nm CMOS process, the pixel array consists of 256 × 256 pixels with 6.5μm pixel pitch. Pixel circuitry is modified based on our previous work and consists of three parts: a 4T pixel, an exposure control (EX) gate and an in-pixel static random access memory (SRAM) block. The 4T pixel include a pinned-photodiode (PD), a transfer gate (TX), a reset gate (RST) and a row selection gate ($RSEL$) [10], [13]. We inserted the EX gate between PD and the readout circuitry for pixel-wise exposure control. An in-pixel 1-bit static random access memory (SRAM) block controls the EX gate to modulate pixel-wise exposure according to the timing diagram in Fig. 4 and Fig. 5.

Unlike our previous design where EX is placed between PD and TX [10], in this design the EX gate is inserted between TX and FD instead. As we shall elaborate in the next section, this modification fixes sampling deadtime caused by charge dissipation that was present in our previous design.

On the chip level, we use analog correlated double sampling (CDS) and cyclic ADCs for column readout. Compared to successive approximation register (SAR) ADC used in our previous work, the cyclic ADC occupies less area by minimizing the use of on-chip capacitors [14], [15]. The schematic and timing of the ADC are shown in Fig. 3. The operational transconductance amplifier (OTA) is shared between the CDS circuit and ADC. We choose a single-ended architecture over the fully differential one to further save chip area. Each cyclic ADC's layout has dimension of 6.5$\mu m \times$ 200μm to fit into the pixel column pitch.

Pixel-wise exposure control is done through the SRAM drivers located at the bottom of each column. When a row is selected for readout through $RSEL$, these SRAM drivers are loaded with the exposure bits for all the pixel within that row. The timing for SRAM writing procedure is explained in the next subsection.

2) Timing: The circuit timing diagram is shown in Fig. 4 for a pixel located at row zero and column one. When this row is selected for readout, we pre-charge the BIT line for this column ($BIT[1]$) to high, indicating this pixel is ending

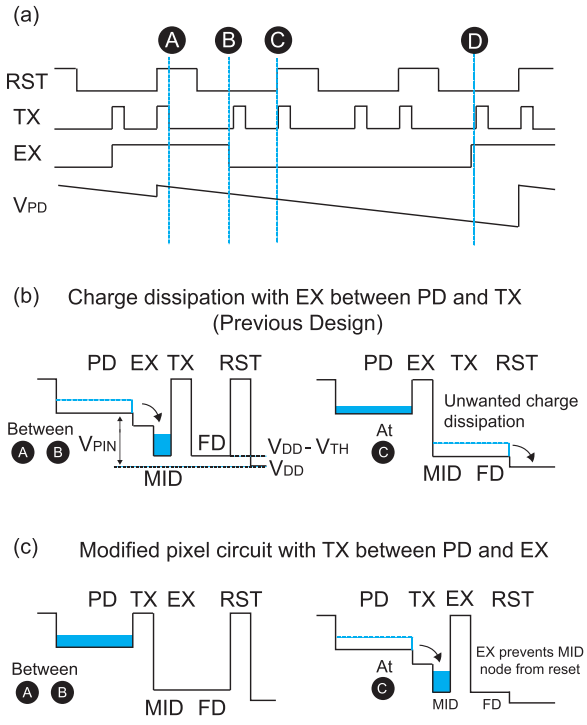

Fig. 5. Timing diagram and pixel charge transfer: (a) pixel timing diagram across multiple frames (b) charge transfer plot of pixels in our previous design [10] (c) charge transfer plot of modified pixels in this work.

its exposure. The CDS circuit then samples the reset value onto C_1, while putting voltage $V_{RP} - V_{COM}$ across C_2. The $WORD$ line for row zero ($WORD[0]$) subsequently pulses to write the SRAM with the logic value of BIT. This turns $EX[0, 1]$ gate ON, connecting PD to the readout structure. Then TX pulses to transfer light generated charge from the PD onto the FD node. FD voltage is subsequently sampled onto C_1 while C_2 is place in the feedback path of the amplifier. At the end of the CDS signal phase, the voltage, V_{OUT}, is:

$$V_{OUT} = \frac{C_1}{C_2}(V_{RESET} - V_{SIGNAL}) + V_{RP} \tag{1}$$

where V_{RESET} is the FD reset value and V_{SIGNAL} is FD signal value after charge transfer. V_{RP} is the voltage to adjust V_{OUT} into the proper ADC dynamic range. Note that the CDS's reset sampling must occur before EX is programmed to release charge onto the FD node.

Analog to digital (AD) conversion begins after the conclusion of CDS. We divide the digitization process into two repeating sub-phases driven by two non-overlapping clocks (ϕ_1 and ϕ_2). During the sampling sub-phase, the ADC samples the output of the OTA onto the capacitor C_1 and C_2. Then during the amplification phase, it drives V_{OUT} to the value given by:

$$V_{OUT} = 2V_{OTA} - V_R \tag{2}$$

where V_R is determined by the 1.5-bit MDAC based on the output of the sub-ADC:

$$V_R = \begin{cases} V_{RH}, & \text{if } D = 2 \\ V_{COM}, & \text{if } D = 1 \\ V_{RL}, & \text{if } D = 0 \end{cases} \tag{3}$$

The MDAC generates 1.5-bit per conversion stage. This is a widely used technique in pipeline/cyclic ADC design to relax sub-ADC's comparators precision [14], [15]. The ADC repeats sampling and amplification sub-phase ten times. Addition logic then generates 10-bit digital output based on each stage's results and transmit the digital word to a serial interface for readout.

3) Modified Pixel Design: Fig. 5(a) shows the pixel timing across multiple frames and charge potential diagrams to illustrate charge transferring at key timing point. We use this figure to illustrate the sampling deadtime present in our previous design, and our design modification in this paper.

To end this pixel's previous exposure, we pull EX signal high to sample the pixel. This pixel potential is then reset at timing point A. The EX remains high until this pixel is selected at the next frame at timing point B. In our previous design [10], where EX is inserted between PD and TX, the photo-generated charges will pour into MID when EX is high between timing A and B (Fig. 5(b)). These charges would then be trapped at MID when EX is pulled low at point B, and subsequently cleared when TX and RST are pulled high at timing point C. Therefore, these charges would be absent when the pixel value is readout at the end of exposure (timing point D). With this charge dissipation, the final charge measured at point D are the ones collected between B and D, but we lose the ones collected between A and B. But since MID's well-potential is much smaller compare to FD and PD, this non-ideality can be negligible in bright light conditions.

Aiming to fix this issue, we switch the location of EX and TX gate such that TX is placed between PD and EX (Fig. 5(c)). Between timing point A and B, the charges are kept at PD since TX is always high. At timing point B, EX is pulled high before TX to rise the potential barrier. The subsequent TX pulses would transfer the charges onto the MID node, which would be protected from reset by the EX potential barrier, shown at timing point C. At timing location D, EX is lowered to allow this pixel to be sampled. Note that during CDS, we sample the reset prior to lowering EX. Therefore, the charges trapped at MID would be counted as the signal voltage. The resulting sample at point D would the charges collected between point A and D.

B. Chip-Computer Bi-Directional Interface

To prototype pixel exposure control algorithms, it is convenient to work with a high level language running on a computer. However, with a computer in the loop it is imperative to minimize communication delay times to prevent closed-loop instability. To achieve single frame delay in the exposure control, we must minimize the communication delay from the chip to computer so more time can be allocated to the exposure control algorithms on the computer side. We have selected the PCIe bus for chip-computer communication due to its high bandwidth and low transmission latency. We implement the bi-directional PCIe interface using a Xilinx Kintex-7 FPGA with IP cores from Xillybus [16]. We characterized the round-time communication delay to average around $70\mu s$, with maximum delay of $85\mu s$ [17]. This makes communication

speed negligible to time between two frames (for framerate <100 FPS, time between frames is >10ms).

In addition to hosting the bi-directional PCIe interface, the same Kintex-7 FPGA also implements logic to convert pixels' exposure values from the computer to serial data streams. These data streams are then sent to the image sensor to load the shift registers at the input of the SRAM drivers, shown in Fig. 3.

To rapidly prototype different feedback control algorithms, we made use of the Bonsai visual programming language [18]. We developed Bonsai plugins on top of a data streaming API [19]. Specifically, we developed a source plugin (PCE-CameraRead) to capture images from the camera and a sink (PCECameraWrite) to write pixel exposure times to the camera using the bi-directional PCIe link. Code for these plugins is available on the Bonsai.CodedPixel git repository (https://github.com/jonnew/Bonsai.CodedPixel). Bonsai includes many high performance image processing components and easy to use stream synchronization elements making it ideal for our purposes. Bonsai workflows implementing for each of the control algorithms presented in this paper can be found in the algorithms folder of the CodedPixel git repository.

C. Pixel-Wise Exposure and Sample Rate Controller

For prototyping, the pixel-wise exposure controller is hosted on a computer linked to the image sensor using the PCIe interface. By controlling pixel-wise exposure, the controller can also adjust each pixel's sampling rate. The goal of the controller is to optimize pixel exposure based on estimates of local intensity and motion information. Pixel exposure should be adjusted to avoid overexposure, underexposure and motion blur. We divide this optimization task into two control modes: exposure optimization based on (1) intensity and (2) local scene motion.

1) PI Mode: Exposure Optimization Based on Intensity: We used a proportional integral (PI) controller to control pixel exposure based on its intensity measurement. The goal is to maintain the intensity of each pixel, $I_{x,y}$ within a desired range that is set just below the point of over-exposure, similar to [2]. To define this controller, we first calculate an intensity error for every pixel:

$$\epsilon_{x,y} = \begin{cases} I_{x,y}(n) - I_{target}, & \text{if } |I_{x,y} - I_{target}| > e_{tol} \\ 0, & \text{otherwise} \end{cases} \quad (4)$$

where $\epsilon_{x,y}(n)$ is the intensity error for pixel at row x and column y. I_{target} is a constant representing the desired intensity. The positive constant, e_{tol}, is an error tolerance such that $\epsilon_{x,y}(n)$ is non-zero only when $|I_{x,y} - I_{target}|$ is larger than e_{tol}. With the error term defined, the PI controller is written as:

$$r_{x,y}(n) = K_p \epsilon_{x,y}(n) + K_i \sum_{n'=0}^{n} \epsilon_{x,y}(n') \quad (5)$$

$$E_{x,y}(n) = \lfloor E_{x,y}(n-1) - r_{x,y}(n) \rfloor \quad (6)$$

where $r_{x,y}(n)$ is the output of the PI controller. K_p and K_i are the proportional and integral gain respectively. Finally, the pixel exposure value, $E_{x,y}(n)$, is an integer representing the multiples of the shortest exposure. We calculate the $E_{x,y}(n)$ as the numerical floor of the difference between the previous exposure $E_{x,y}(n)$ and $r_{x,y}(n)$. the PI controller will minimize $r_{x,y}(n)$ to achieve steady state $E_{x,y}(n)$ and $I_{x,y} \approx I_{target}$.

There are four parameters to set for the PI controller: I_{target}, e_{tol}, K_p and K_i. The choice of these parameters depends on the pixel intensity range and the max allowable $E_{x,y}(n)$. For example, if $1 \leq E_{x,y}(n) \leq 8$ and in a standard image format where pixel value range from 0 - 255, I_{target} can be selected to be around 200, with e_{tol} of 30. That means the PI controller will try to keep optimal pixel in the range between 170 to 230. We should increase K_p to speed up settling. Its value should not be too larger to induce instability. K_i should be kept as a small fraction of K_p to eliminate residual error after the application of the proportional control. We select these gain parameters using the following rule:

$$K_p < \frac{max(E_{x,y})}{max(\epsilon_{x,y})} \quad \text{and } K_i < 0.1\dot{K}_p \quad (7)$$

where K_p should be less than the quotient of maximum exposure and intensity error, and K_i should be less than 10% of K_p. This parameter selection ensures that in most extreme condition $r_{x,y}$ does not cause $E_{x,y}$ to overshoot and create instability. In this example, if I_{target} is 200, then K_p should be less than $8/170 = 0.04$ and K_i should be less than 0.004.

In the previous work, the light illuminance control algorithm proposed by Nayer and Branzoi is based on a proportional controller [2]. The lack of integral gain may lead to steady state error during operation. To illustrate this, we constructed a numerical simulation of a single pixel, shown in Fig. 6. In this example, PI controller parameters are set as: $I_{target} = 800$, $e_{tol} = 50$, $K_p = 0.003$. The incident light intensity at this pixel changes from 800 to 100 at $n = 100$. We plot two situations when $K_i = 0$ and $K_i = 0.001$ to mimic the controller by [2] and our work.

The light intensity, error term ($\epsilon(n)$), PI controller output ($r(n)$) and exposure length ($E(n)$) are plotted in columns of Fig. 6. This pixel is at equilibrium with $E(n) = 1$ until $n = 100$, when the light intensity decreases from 800 to 100. This causes the error $\epsilon(n)$ to grow, and the controller increases $E(n)$ to compensate. When $\epsilon(n)$ terms decrease beyond threshold, it causes the proportional effect to diminish. This seems reasonable. However, as we see in Fig. 6. the rounding of continuous controller output to discrete value of $E(n)$ introduces steady-state error $\epsilon(n)$. This error cannot be eliminated in the absence of K_i. Thus, when K_i is set to 0, exposure length, $E(n)$, cannot increase beyond 5. This leads to a sustained large $\epsilon(n)$.

This steady-state error can be eliminated in our PI controller, when K_i is non-zero. ϵ(n) gets integrated and causes $r(n)$ to further push $E(n)$ to the optimal value of 8, which eliminates ϵ(n), shown on the right column of Fig. 6.

2) OF Mode: Exposure Optimization Based on Motion: Pixel exposure should not only depends for light intensity, but also motion. It is optimal to use short pixel exposure and fast frame rate to minimize motion blur and to avoid

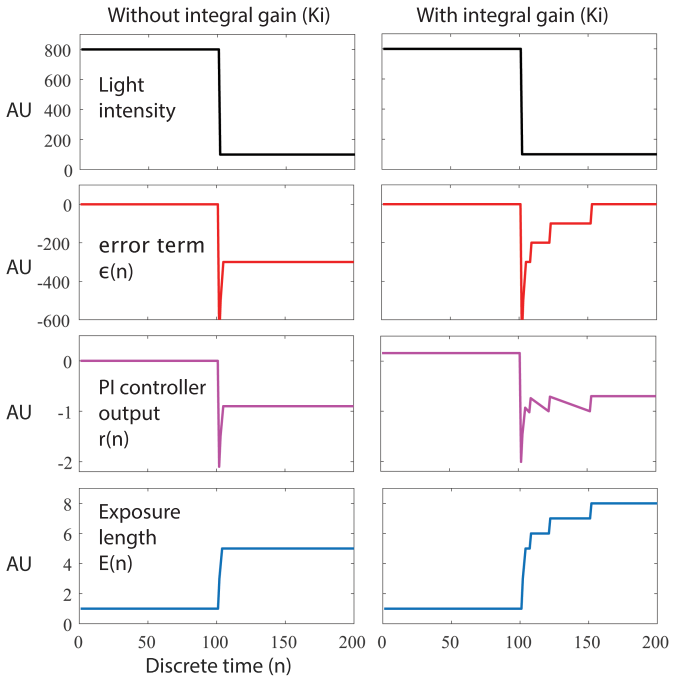

Fig. 6. Simulation of a single pixel's behavior in PI mode. The left column shows the incoming light intensity and PI controller parameters for zero integral gain (K_i). The right column show the same pixel's behavior with non-zero K_i.

temporal aliasing. Here we describe the OF mode controller that tunes pixel exposure preemptively by estimating local motion using optical flow (OF) measurements [20], [21].

We first tried to combine OF mode controller with the PI mode controller, but OF-based control introduces some issues into the PI controller. First, for a static scene, when we change exposure at $E(n-1)$ using the PI controller, it results in non-zero optical flow vectors computed at time t due to the pixel intensity change. This "false" OF value is representative of our control signal — not the actual motion of in the scene — and therefore could cause errors on motion driven exposure optimization. Second, OF measurement can be noisy at the pixel level, especially at low light condition with low SNR. Furthermore, OF measurements' accuracy can also be affected by motion blur caused by long exposures. All of these factors make pixel-wise motion driven exposure difficult to achieve.

To address these issues, we allow the PI controller and the OF controller to engage pixels separately depending on the magnitude of pixel motion. We first divide the image into sub-blocks of size $M \times M$ pixels. We then calculate the average OF for all the pixels within each of these blocks over a period of time, T_{switch}:

$$\upsilon_{i,j}(n) = \frac{1}{M^2 \dot{T}_{switch}} \sum_{y=1}^{M} \sum_{x=1}^{M} \sum_{n'=n-T_{switch}}^{n} |u_{x,y}(n')| \quad (8)$$

where $|u_{x,y}|$ is magnitude of the optical flow vector at pixel (x, y). $\upsilon_{i,j}$ is the average of $|u_{x,y}|$ over a period T_{switch} for all the pixels within this block. Spatially averaging of OF enhances measurement accuracy, while temporal averaging over a period of T_{switch} allows us to distinguish motion from instantaneous change in pixel value due to closed-loop exposure updates. After incorporating $\upsilon_{i,j}(n)$, pixel exposures are determined as:

$$E_{x,y}(n) = \begin{cases} E_{PI_{x,y}}(n), & \text{if } \upsilon_{i,j} < \upsilon_{tol} \text{PI} \\ \lfloor max(E_{x,y}) - K_\upsilon \upsilon_{i,j} \rfloor, & \text{if } \upsilon_{i,j} \geq \upsilon_{tol} \text{ OF} \end{cases} \quad (9)$$

υ_{tol} is a constant threshold to determine controller mode selection. For static regions or regions with instantaneous motion, we allow PI mode to control pixel exposure. For regions with constant motion, we use OF mode which calculates exposure based on the magnitude of the motion. K_υ is the gain that converts the OF magnitude, measured in units of pixels moved, to exposure values. K_υ was determined using test images, where lines are moved in front of the camera at different speed to determine the correct K_υ to avoid motion blurring.

IV. Experiments

We next experimentally investigated the adaptive exposure feedback imaging system. In all the experiments described here, $E_{x,y}$ is represented by a 3-bit integer. $E_{x,y} = 1$ corresponds to shortest pixel exposure of 30 ms, while longest exposure $E_{x,y} = 8$ corresponds to pixel exposure of 240 ms. This setting also configures the fastest pixel sampling rate to around 30 frames per second (FPS) and slowest sampling rate to around 4 FPS. Before the raw images from the sensor is sent to the exposure controllers, they first undergo fixed-pattern noise correction and are filtered by a 3×3 median filter to remove salt-and-pepper noise from defected pixels.

In these experiments, we take the 10-bit ADC full scale as pixel's value range $(0 - 1024)$. We set the PI controller parameter following equation (7): $I_{target} = 800$, $\epsilon_{tor} = 120$, $K_p = 0.01$ and $K_i = 0.001$. We compute the OF measurements using the Farnelback method based on polynomial expansion [20]. We set $K_\upsilon = 2$, this means for every motion magnitude $\upsilon_{x,y}$ of 1 pixels, we reduce exposure, $E_{x,y}$, by 2 steps. M is set to be 8 corresponding to $\upsilon_{x,y}$ averaging over an 8×8 blocks.

A. Setup

Fig.7 shows the chip micrograph, the data collection setup, and two scenes used for experiments. The chip is wirebonded onto the PCB and mounted behind an objective lens, shown in Fig. 7 (a) and (d). The data from the image sensor is transmitted to a connector board which sends the data into the KC705 FPGA its FPGA Mezzanine Card (FMC) port, shown in Fig.7(b). The KC705 hosts the PCIe bi-directional interface and is mounted onto one of computer's PCIe slots. Fig. 7(c) is a scene used in this experiment. It is a cardboard cutout in a shape of a cartoon sun. We overlay it with a transparent paper with a drawing of a smiley face. This setup is then back-illuminated to create high dynamic range scene for imaging experiment. Fig.7(d) is a setup to create continuous motion to test the functionality of the controller in OF mode. Objects are mounted on a rotating stand. The spinning then creates continuous motion at the top-half of the video, while the bottom half remain stationary.

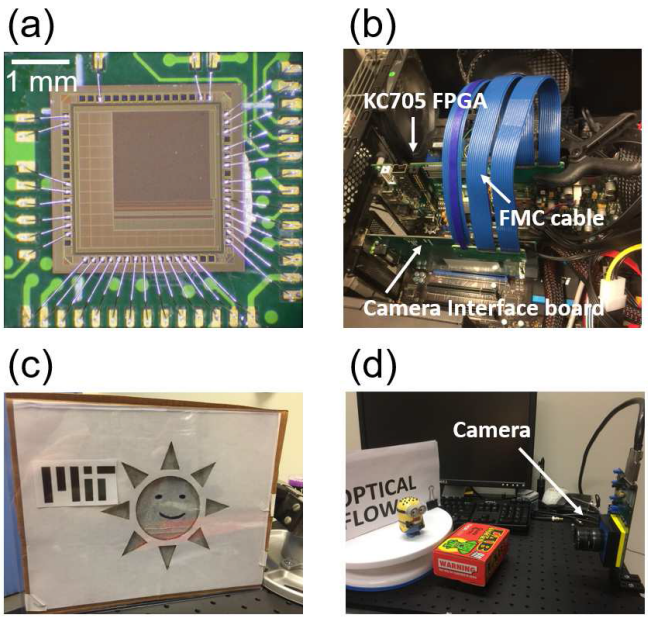

Fig. 7. Chip micrograph and experimental setups: (a) chip micrograph (b) data collection setup (c and d) scenes and objects used for testing the PI controller and OF controller.

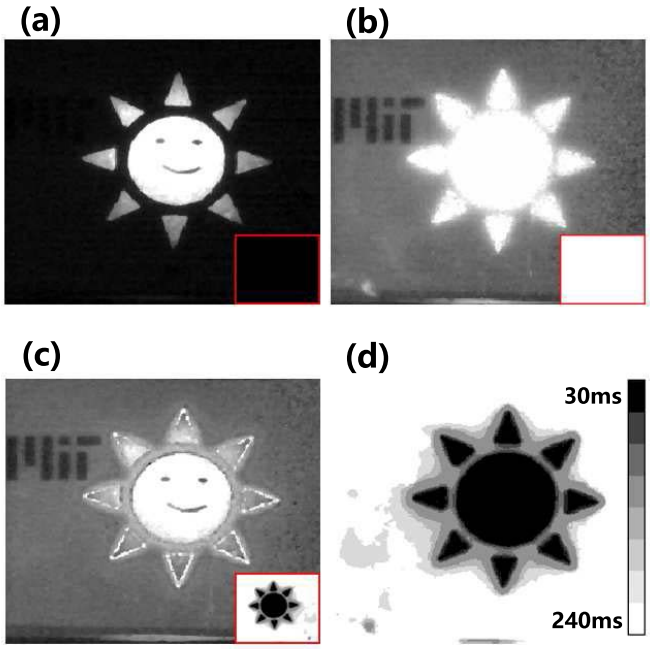

Fig. 8. Pixel-wise exposure optimization for stationary scene using controller in PI mode. Pixel exposure patterns are shown in the red box of the corresponding subfigure. (a) Image acquire with short global exposure, (b) long global exposure. (c) Image acquired with optimized pixel-wise exposure set by the PI controller. (d) enlarged pixel-wise exposure pattern in (c) where pixel exposure are indicated in the legend of (d).

All examples in the experiment are processed in real-time. The closed-loop exposure processing and feedback algorithm is implemented on a PC (CPU: Intel Core-i7 Quad-core 8 threads). It is written with C# using Bonsai API. The processing time is $< 10\ ms$, while the maximum round trip data delay of the PCIe interface is $< 85\mu s$. The detailed experiment results are described in the next sections.

B. Stationary Scenes

Fig. 8 shows a back-illuminated pictures of a cartoon cardboard cutout in the shape of a sun under different exposure settings. In Fig. 8(a) and (b), the entire scene undergoes short (30ms) and long (240ms) global exposures respectively. During short exposure, the smiley face overlaid on top of the circle, and the gap between the circle and the triangle cutouts are visible and can be easily segmented. However, the background remains dark. Conversely, during long exposure, the background text of the MIT logo is visible, but the circle and triangles parts of the sun are over-exposed. As a result, the edges between the shapes shrinks due to over-exposure. This makes the segmentation more difficult. In addition, due to over-exposure, the smiley face is entirely saturated.

Fig. 8(c) shows an example when each pixel's exposure is tuned based on its intensity using the pixel-wise exposure controller as described in section III.C. Since the camera is imaging a static scene, the control adjusts pixel-wise exposure in PI mode. The pixel-wise exposure for generating Fig. 8(c) is shown in (d). The controller sets most of the background to long exposure of 240ms to enhance the SNR. It only lowers the exposure values for pixels within the back-illuminated circle and triangles to avoid over-exposure. The pixels around the bright regions are tuned to have exposure between 30ms and 240ms. As a result, both the background text and the smiley face at the back-illuminated region are visible. The gaps between the circle and triangles are also wide and distinguishable.

C. Motion Scenes

1) Instantaneous Motion: Fig. 9 demonstrates the controller's performance for scenes with instantaneous motion. We show two examples here. For each example, we plot the image sensor output on the top row and the corresponding pixel exposure pattern on the bottom row. In the example (a), we move the back-illuminated cardboard cutout to the right at frame 2. This motion is not large enough to cause the controller to switch to OF mode from PI mode. As a result, pixels in the region where the motion occurs become overexposed and underexposed. This causes the error function to grow and PI controller starts to regulate pixels exposure, shown in frame 3 and 4. The pixels' exposure eventually settles at frame 5, after 3 frames following the end of motion

Fig. 9(b) shows another example, where an incandescent light bulb is placed in front of an MIT logo. The PI controller tunes the pixels at bulb's filament to short exposure while keeping the background at longer exposures. This enables us to see both the shape of the filament and background. We then introduce motion at frame 2 and 3 by moving the bulb right. Pixels at the motion region become sub-optimally exposed. The PI controller starts to engage, and cause they pixels exposures to quickly settle to new values at frame 6.

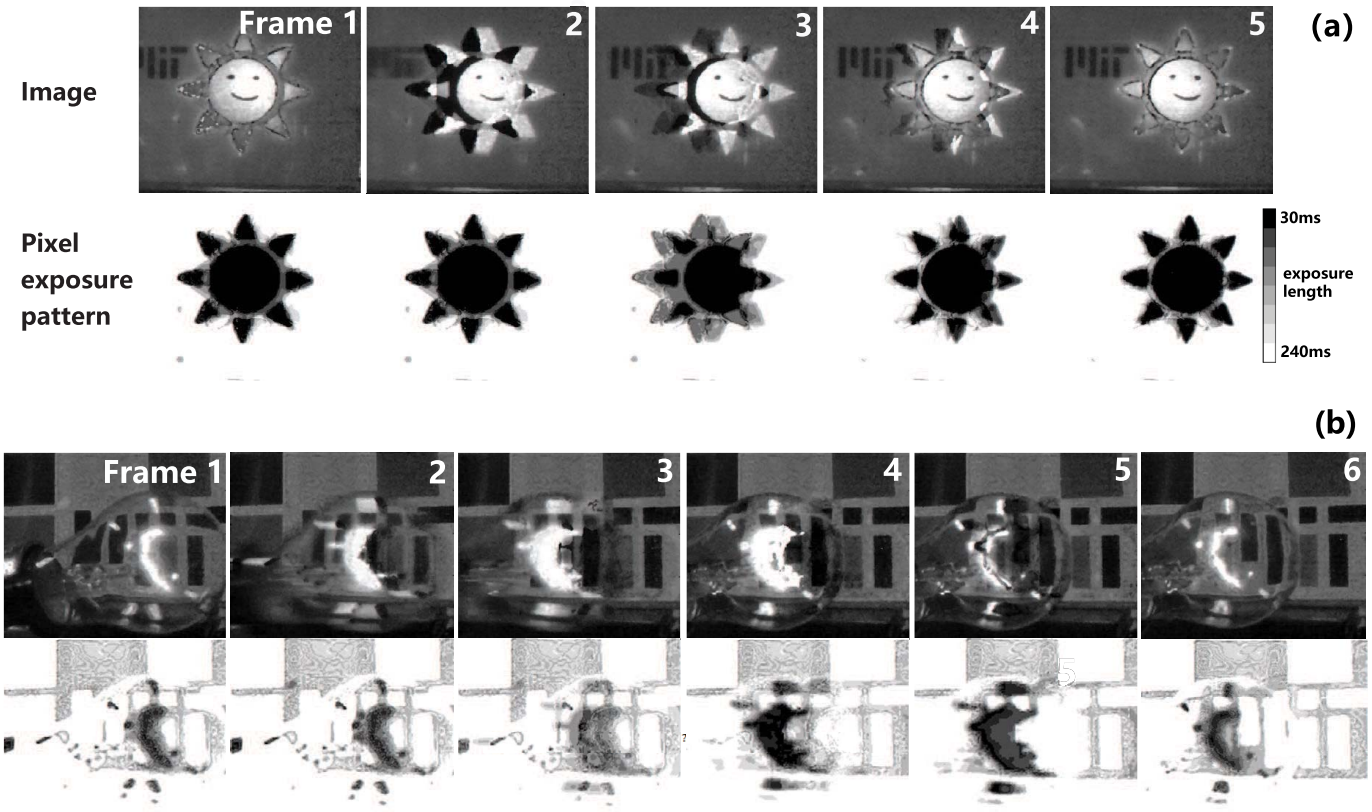

Fig. 9. Pixel-wise exposure optimization for scenes with instantaneous motion using the controller in PI mode. Two video examples are shown in (a) and (b). The top row of each example shows the image sensor output, while the bottom row shows the corresponding pixel exposure pattern. The legend for pixel exposure length is also.

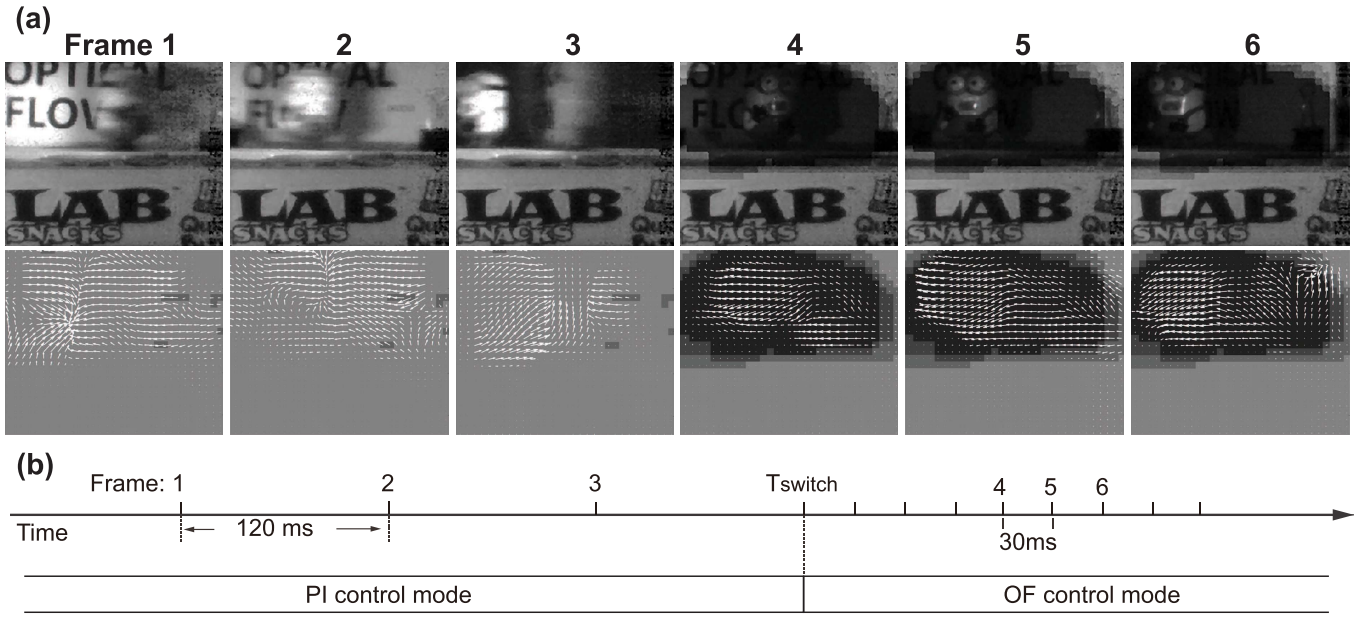

Fig. 10. Pixel-wise exposure optimization for scenes with continuous motion using controller in OF mode. (a) Six frame from a video where image sensor outputs are shown in the top row, while pixel exposure patterns and OF measurements are shown in the bottom row. (b) A timeline showing the duration between each frames. Frame 1-3 are captured 120 ms apart, while the upper pixels in frame 4-6 are captured 30ms apart. When pixels' exposure are shorten at T_{switch}, the pixel sampling rate also increases in the corresponding region.

2) Continuous Motion: Fig. 10 demonstrates an example where a continuous motion triggers the OF mode for pixel exposure control. In this example, objects are placed on a rotating stand, as shown in Fig. 9(c). We then spin the stand to

TABLE I
CHIP CHARACTERIZATION AND COMPARISON

	[12]	[11]	This work
Process	110nm CIS	130nm CMOS	130nm CMOS
VDD (V)	-	2.5	1.5
Pixel architecture	APS	CTIA	APS
Pixel pitch (μ m)	11.2	12.2	6.5
Fill factor (%)	45	33	54
Array size	244×162	10×10	256×256
In pixel memory	2 latches	2 DRAM	1 SRAM
Max FPS	25	60	100
FPN@Dark (%)	-	0.18	1.41
FPN@50% Sat. (%)	-	-	1.77
Read noise @Dark (DN)	-	-	see Fig.11
Power (mW)	34.4	1.23	7.31
Power FOM (nJ)*	34	205	1.12

*: FOM = Power/(Number of Pixels) × (Frame rate))
-: not available

generate a continuous motion on the top section of the video frame, while the bottom section remains stationary.

Fig. 10(a) top row shows the outputs of the image sensor, while the bottom row shows pixel exposures and corresponding OF vectors. Initially, each pixel is configured to have relatively long exposure of 120ms with sample rate of 8 FPS. At long exposures, the sampled frames have good SNR but surfers from blurring effects as shown in frame 1 to 3 of Fig. 10.

As the motion persists, the optical flow measurements are continuously integrated according to equation (8), and for some patches it reaches the threshold v_{tol} at end of period T_{switch}. This causes the controller to switch from the PI mode to the OF mode for patches with continuous motion, according to equation (9). In OF mode, the pixel exposures are then optimized according to the magnitude of velocity instead of intensity. In this example, it shortens pixel exposure and increase frame rate for the top region of the frame for the amount proportional to the magnitude of the OF vectors. These pixels now update every $30ms$ instead of $120ms$ and resulting in blur-less capturing of the motion, shown in frame 4 to 6.

It can also be observed that the OF measurements in frame 1-3 are less accurate in reflecting the true motion due to the blurring effects from long exposures. In this example, the objects are spinning in front of the camera with a constant motion. All the pixels in motion should have OF measurements pointing to the same direction. But due to blurring in frame 1-3, some patches' OF vectors are incorrectly computed resulting in the large variance of estimated motion directions. This is compared to OF measurements in frame 4 to 6, where blurless frames also result in more accurate motion estimations.

V. MEASUREMENTS AND COMPARISON

The measurement results of our sensor is listed in Table I and compared with previous works by Sarhangnejad et al. and Luo, Ho and Mirabbasi on pixel-wise coded exposure [11], [12]. Using active-pixel sensor (APS) architecture with single-tap readout, our sensor can achieve better fill factor and smaller pixel size. Our work has higher fixed pattern noise (FPN) due to layout technique to maximize fill factor and the use of a non-CMOS image sensor (CIS) process. The read noise of the sensor is plotted in Fig. 11. The increase in noise with respect to exposure is due to the presence of dark current. This is expected as the additional floating diffusion (MID) contributes to extra dark current, similar to global shutter image sensors.

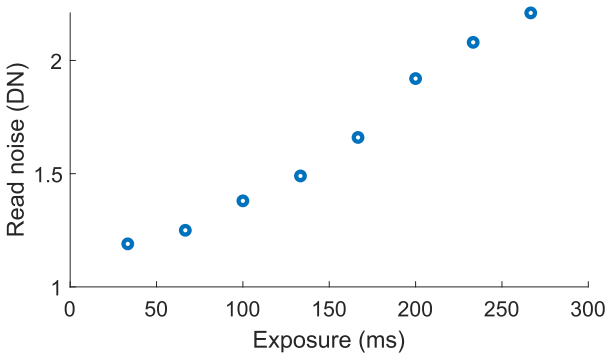

Fig. 11. Sensor read noise at dark plotted with exposure length, measured in digital number (DN) rms.

Table II summarizes our work with respect to other alternatives: address-event sensors [22]–[24], logarithmic sensors [25], [26], and optical illumination modulation with a conventional APS image sensor [2], [3]. This table offers a qualitative comparison of some key specifications: dynamic range, speed, noise/SNR and power.

A. Dynamic Range

All four types of sensors can achieve HDR but limitations for their dynamic range varies. Pixel-wise exposure sensors use short exposure to capture high light, therefore the limitation to their DR is the shortest exposure time, which is determined by the readout circuitry and photodiode charge transfer time. Address-event sensors convert photocurrent into frequency. Thus, at high light, its DR is limited by the maximum speed of address-event representation (AER) transceiver. Logarithmic sensors compress the photocurrent into a logarithmic behavior of the transistor subthreshold current. Their DR is limited by the biasing condition of the transistor. Finally, the DR of the optical modulation is dependent on the resolution and accuracy of the SLMs.

B. Speed

The speed of the pixel-wise exposure sensor and the logarithmic sensors are comparable due to the use of row select column readout. AER sensor can achieve the fastest speed due to its asynchronous architecture. Optical modulation is the slowest because its speed is further constrained by SLMs' speed.

C. Noise/SNR

Pixel-wise exposure sensor achieves the best noise and SNR performance. The integration of charge in the photodiode minimizes shot noise and the use of CDS further reduces read noise. Pixel-wise exposure sensor can further improve SNR

TABLE II
QUALITATIVE COMPARISON WITH OTHER HDR IMAGING SYSTEMS

	Pixel-wise exposure sensors (this work)	Address-event sensors [22] [23] [24]	Logarithmic sensor (this work) [25] [26]	Optical modulation [2] [3]
Dynamic Range (DR)	**High** At high light, DR is limited by shortest possible exposure.	**High** At high light, DR is limited by speed of the AER link	**High** At high light, DR is limited by VGS of subthreshold transistor	**High** DR is limited by the optical modulator [6ex]
Speed	Medium Speed is limited by column readout circuits	**High** Speed is limited by speed of AER	Medium Speed is limited by column readout circuits	Low Speed is fixed by the column readout
Noise / SNR	**Low / High** Speed is limited by column readout circuits	High / Low Speed is limited by speed of AER	High / Low Speed is limited by column readout circuits	Low / Medium Speed is fixed by the column readout
Power	**Low** APS based architecture ensure low power	Variable Variable power consumption depending on activity of AER communication	High Due to constant subthreshold current leakage.	High It uses additional optical modulation device in addition to image sensor

by extending exposure duration. AER and logarithm sensors achieve inferior noise and SNR performance. For AER, fabrication process variation leads to high FPN due to mismatch in the event thresholds. The difficulty of using time-domain CDS further leads to higher read noise. Similar problems exist in logarithmic sensors where device mismatch and lack of CDS leads to increased FPN and read noise. The measurement of photocurrent directly without charge integration also leads to higher shot noise. The optical modulation should achieve good noise performance due to the use of conventional APS sensor. However, the sensor's frame rate is fixed, thus optical systems cannot prolong exposure adaptively to improve SNR.

D. Power

Pixel-wise exposure sensor has the lowest power due its APS based pixel architecture. AER sensor has variable power consumption depending on pixel spiking rate. Logarithmic sensors have high power consumption due to constant leakage of subthreshold current. Optical modulation also has high power consumption due to additional SLMs.

VI. CONCLUSION AND FUTURE WORK

We have demonstrated an imaging system with closed-loop pixel-wise exposure control. In addition, we provided control algorithms (PI and OF mode) to tune each pixels exposure and sampling speed according to local intensity and motion information. Overall, the pixel-wise imaging system is effective at minimizing motion blur, under- and overexposure due to suboptimal pixel exposure, and outperforms conventional frame-base image sensors at acquiring scenes with large variance in brightness and motion.

Our current system uses a PCIe based communication protocol and high-level software in the control loop for prototyping purposes. In the future, we foresee the complete integration of the control logic into the camera sensor to form an SoC capable of native and automatic adaptive pixel exposure control. In addition, several areas of the system could also be improved in future works:

A. Application Dependent Metrics for Measuring Sub-Optimally Sampled Pixels

The key to high performance controller is well-defined error functions. In our controller, we used intensity error to measure over and under exposure, and in addition used optical flow as an indicator for motion blur. These performance metrics are selected for general applications. A better approach would be to find application dependent metric to measure sub-optimally sampled pixels. For example, when the videos are inputs to classification or segmentation tasks, we could use classification or segmentation accuracy as a metric to adjust exposure and frame rate.

B. Combining Learning to Pixel-Wise Exposure Estimation

The recent development in convolutional neural network (CNN) could also be utilized to learn the optimal pixel exposure patterns. Previous work using CNN for optical flow estimation and motion blur detection and removal have been proposed [27]–[29]. A similar network architecture could be used to segment the scene based optical pixel exposure. A potential difficulty with this approach is the collection of high dynamic range and multi-frame rate video data for network training.

REFERENCES

[1] E. R. Fossum, "CMOS image sensors: Electronic camera-on-a-chip," *IEEE Trans. Electron Devices*, vol. 44, no. 10, pp. 1689–1698, Oct. 1997.
[2] S. K. Nayar and V. Branzoi, "Adaptive dynamic range imaging: Optical control of pixel exposures over space and time," in *Proc. 9th IEEE Int. Conf. Comput. Vis.*, Oct. 2003, pp. 1168–1175.
[3] M. D. Tocci, C. Kiser, N. Tocci, and P. Sen, "A versatile HDR video production system," *ACM Trans. Graph.*, vol. 30, no. 4, p. 41, Jul. 2011.

[4] P. J. Burt and R. J. Kolczynski, "Enhanced image capture through fusion," in *Proc. 4th Int. Conf. Comput. Vis.*, Dec. 2002, pp. 173–182.
[5] T. Mitsunaga and S. K. Nayar, "Radiometric self calibration," in *Proc. IEEE Comput. Soc. Conf. Comput. Vis. Pattern Recognit.*, vol. 1, Jan. 2003, pp. 374–380.
[6] S. Mann and R. Picard, "On being 'Undigital'with digital cameras: Extending dynamic range by combining differently exposed pictures," *MIT Media Lab Perceptual*, vol. 1, p. 2, Mar. 1994.
[7] M. Aggarwal and N. Ahuja, "Split aperture imaging for high dynamic range," *Int. J. Comput. Vis.*, vol. 58, no. 1, pp. 7–17, Jun. 2004.
[8] S. K. Nayar and T. Mitsunaga, "High dynamic range imaging: Spatially varying pixel exposures," in *Proc. IEEE Conf. Comput. Vis. Pattern Recognit. (CVPR)*, vol. 1, Nov. 2002, pp. 472–479.
[9] Y. Y. Schechner and S. K. Nayar, "Generalized mosaicing," in *Proc. 8th IEEE Int. Conf. Comput. Vis. (ICCV)*, vol. 1, Nov. 2002, pp. 17–24.
[10] J. Zhang, T. Xiong, T. Tran, S. Chin, and R. Etienne-Cummings, "Compact all-CMOS spatiotemporal compressive sensing video camera with pixel-wise coded exposure," *Opt. Express*, vol. 24, no. 8, pp. 9013–9024, Apr. 2016.
[11] Y. Luo, D. Ho, and S. Mirabbasi, "Exposure-programmable CMOS pixel with selective charge storage and code memory for computational imaging," *IEEE Trans. Circuits Syst. I, Reg. Papers*, vol. 65, no. 5, pp. 1555–1566, May 2018.
[12] N. Sarhangnejad *et al.*, "Dual-tap pipelined-code-memory coded-exposure-pixel CMOS image sensor for multi-exposure single-frame computational imaging," in *IEEE ISSCC Dig. Tech. Papers*, Feb. 2019, pp. 102–104.
[13] E. R. Fossum and D. B. Hondongwa, "A review of the pinned photodiode for CCD and CMOS image sensors," *IEEE J. Electron Devices Soc.*, vol. 2, no. 3, pp. 33–43, May 2014.
[14] M. Mase, S. Kawahito, M. Sasaki, Y. Wakamori, and M. Furuta, "A wide dynamic range CMOS image sensor with multiple exposure-time signal outputs and 12-bit column-parallel cyclic A/D converters," *IEEE J. Solid-State Circuits*, vol. 40, no. 12, pp. 2787–2795, Dec. 2005.
[15] J.-H. Park, S. Aoyama, T. Watanabe, K. Isobe, and S. Kawahito, "A high-speed low-noise CMOS image sensor with 13-b column-parallel single-ended cyclic ADCs," *IEEE Trans. Electron Devices*, vol. 56, no. 11, pp. 2414–2422, Nov. 2009.
[16] *An FPGA IP Core for Easy DMA Over PCIe With Windows and Linux*. Accessed: Feb. 23, 2020. [Online]. Available: http://www.xillybus.com/
[17] J. Newman, J. Voigts, and A. C. Lopez. (May 2016). *Submillisecond Latency Closed-Loop Feedback With PCIe Prototype System*. [Online]. Available: http://www.open-ephys.org/blog/2016/5/6/submillisecond-latency-closed-loop-feedback-with-pcie-prototype-system
[18] G. Lopes *et al.*, "Bonsai: An event-based framework for processing and controlling data streams," *Frontiers Neuroinform.*, vol. 9, p. 7, Apr. 2015.
[19] J. Newman, J. Voigts, J. Zhang, C. PhilDakin, T. M. Yaoyua, and Z. Rosen. (Jun. 2019). *Jonnew/Open-Ephys-PCIe: Release 1.0.0*. [Online]. Available: https://doi.org/10.5281/zenodo.3254431
[20] G. Farnebäck, "Two-frame motion estimation based on polynomial expansion," in *Image Analysis. SCIA 2003* (Lecture Notes in Computer Science), vol. 2749, J. Bigun and T. Gustavsson, Eds. Berlin, Germany: Springer, 2003. [Online]. Available: https://link.springer.com/chapter/10.1007/3-540-45103-X_50#citeas
[21] B. D. Lucas *et al.*, "An iterative image registration technique with an application to stereo vision," Tech. Rep., 1981.
[22] P. Lichtsteiner, C. Posch, and T. Delbruck, "A 128×128 120 dB 15 μs latency asynchronous temporal contrast vision sensor," *IEEE J. Solid-State Circuits*, vol. 43, no. 2, pp. 566–576, Feb. 2008.
[23] C. Posch, D. Matolin, and R. Wohlgenannt, "A QVGA 143 dB dynamic range frame-free PWM image sensor with lossless pixel-level video compression and time-domain CDS," *IEEE J. Solid-State Circuits*, vol. 46, no. 1, pp. 259–275, Jan. 2011.
[24] E. Culurciello, R. Etienne-Cummings, and K. A. Boahen, "A biomorphic digital image sensor," *IEEE J. Solid-State Circuits*, vol. 38, no. 2, pp. 281–294, Feb. 2003.
[25] S. Kavadias, B. Dierickx, D. Scheffer, A. Alaerts, D. Uwaerts, and J. Bogaerts, "A logarithmic response CMOS image sensor with on-chip calibration," *IEEE J. Solid-State Circuits*, vol. 35, no. 8, pp. 1146–1152, Aug. 2000.
[26] L. Lai, C. Lai, and Y. King, "A novel logarithmic response CMOS image sensor with high output voltage swing and in-pixel fixed-pattern noise reduction," *IEEE Sensors J.*, vol. 4, no. 1, pp. 122–126, Feb. 2004.
[27] A. Dosovitskiy *et al.*, "FlowNet: Learning optical flow with convolutional networks," in *Proc. IEEE Int. Conf. Comput. Vis. (ICCV)*, Dec. 2015, pp. 2758–2766.
[28] J. Sun, W. Cao, Z. Xu, and J. Ponce, "Learning a convolutional neural network for non-uniform motion blur removal," in *Proc. IEEE Conf. Comput. Vis. Pattern Recognit. (CVPR)*, Jun. 2015, pp. 769–777.
[29] S. Nah, T. H. Kim, and K. M. Lee, "Deep multi-scale convolutional neural network for dynamic scene deblurring," in *Proc. IEEE Conf. Comput. Vis. Pattern Recognit. (CVPR)*, Jul. 2017, pp. 3883–3891.

Jie (Jack) Zhang (Member, IEEE) received the B.S. and Ph.D. degrees in electrical and computer engineering from Johns Hopkins University (JHU) in 2010 and 2016, respectively. He was an International Scholar with IMEC, Leuven, Belgium, from 2011 to 2012. He is currently a Post-Doctoral Associate with the Department of Brain and Cognitive Sciences, Massachusetts Institute of Technology (MIT), working with Dr. M. Wilson. His current research interests include VLSI for biomedical applications, image sensors, compressed sensing, electrophysiology, functional neural imaging, and neural mechanisms of spatial navigation and memory consolidation. He also builds open-source tools for the neuroscience community. He is a Key Contributor of Open-Ephys.

Jonathan P. Newman received the B.S. degree in bioengineering from SUNY Binghamton, Binghamton, NY, USA, in 2007, and the Ph.D. degree in bioengineering from Georgia Tech, Atlanta, GA, USA, in 2013. In his Ph.D. dissertation, he developed tools and methods for closed-loop optogenetic control of neural circuits in order to resolve the mechanistic basis for a form of homeostatic plasticity known as synaptic scaling. He is currently a Research Scientist working the Laboratory of Dr. Matthew Wilson, MIT. His research is focused on elucidating how the brain consolidates memory during sleep. He serves as a Lead-Engineer and a Board-Member of Open Ephys, a non-profit organization dedicated to developing high-performance open-source tools for brain research. In this capacity, he has developed and disturbed numerous open-source scientific tools which are now in active use in hundreds of labs around the world.

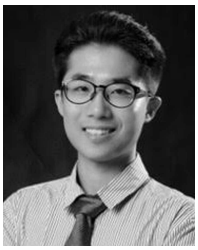

Xiao Wang received the B.S. degree in automation from Shandong University in 2015. He is currently pursuing the Ph.D. degree with the Division of Systems Engineering, Boston University, Boston, MA, USA. During his undergraduate study, he was selected to the brilliance educational program launched by the Ministry of Education of China. He also worked as a Visiting Scholar with Johns Hopkins University in summer 2018. His research interests include adversarial machine learning, AI security, compressed sensing and generative models, and the goal of which is to design deep learning systems with enhanced robustness and compactness.

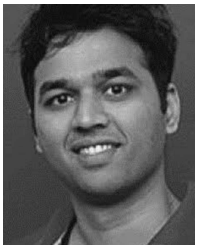

Chetan Singh Thakur (Senior Member, IEEE) received the Ph.D. degree in neuromorphic engineering from the MARCS Research Institute, Western Sydney University (WSU), Australia, in 2016. He has an Adjunct Faculty appointment at the International Center for Neuromorphic Systems, WSU. He then worked as a Research Fellow with Johns Hopkins University. He has extensive industrial experience. He was worked for six years with Texas Instruments Singapore, as a Senior Integrated Circuit Design Engineer, designing IPs for mobile processors. He is currently an Assistant Professor with the Indian Institute of Science (IISc), Bengaluru. His research expertise lies in neuromorphic computing, mixed-signal VLSI systems, computational neuroscience, probabilistic signal processing, and machine learning. His research interest is to understand the signal processing aspects of the brain and apply those to build novel intelligent systems. He was a recipient of several awards, such as the Young Investigator Award from Pratiksha Trust, the Early Career Research Award by Science and Engineering Research Board, India, and the Inspire Faculty Award by Department of Science and Technology, India.

John Rattray (Student Member, IEEE) received the B.S. degree in computer engineering from the University of Maryland, Baltimore County, in 2015, and the M.S.E. degree in electrical and computer engineering from Johns Hopkins University in 2017, where he is currently pursuing the Ph.D. degree. His research focuses on neuromorphic visual saliency and the design of wearable sensor arrays for monitoring patients with traumatic brain injuries. He is also the Founder and the CEO of the startup Sparkwear, Inc. He was awarded the GEM National Fellowship and was recognized as a DARPA Early Riser for his research in neuromorphic visual saliency.

Ralph Etienne-Cummings (Fellow, IEEE) received the B.S. degree in physics from Lincoln University, Lincoln, PA, USA, in 1988, and the M.S.E.E. and Ph.D. degrees in electrical engineering from the University of Pennsylvania, Philadelphia, PA, USA, in 1991 and 1994, respectively. He was the Founding Director of the Institute of Neuromorphic Engineering. He is currently a Professor of electrical and computer engineering, and computer science with Johns Hopkins University, Baltimore, MD, USA. He has authored more than 200 peer-reviewed articles. He holds numerous patents. He has served as the Chairman of the IEEE Circuits and Systems (CAS) Technical Committees. He was elected as a member of CAS Board of Governors. He also serves on numerous editorial boards. He was a recipient of the NSFs Career and Office of Naval Research Young Investigator Program awards. He was a Visiting African Fellow with the University of Cape Town, Fulbright Fellowship Grantee, the Eminent Visiting Scholar with the University of Western Sydney. He has also won numerous publication awards, including the 2012 Most Outstanding Paper of the IEEE TRANSACTIONS ON NEURAL SYSTEMS AND REHABILITATION ENGINEERING. In addition, he was recently recognized as a Science Maker and an African American history archive.

Matthew A. Wilson received the B.S. degree in electrical engineering from Rensselaer Polytechnic Institute, the M.S. degree in electrical engineering from the University of Wisconsin–Madison, Madison, WI, USA, and the Ph.D. degree in computation and neural systems from the California Institute of Technology. He joined the faculty at MIT with the Department of Brain and Cognitive Sciences in 1994. He is currently a Sherman Fairchild Professor of neurobiology. He studies the role of sleep in learning and memory, and brain systems that contribute to spatial navigation, and decision making, and their possible involvement in neurological diseases and disorders through the use of microelectrode arrays implanted in the brains of freely behaving rodents. He is also an Associate Director of The Picower Institute for Learning and Memory, MIT, and an Associate Director of the Center for Brains Minds and Machines.